# Supplementary Information for "Scale interactions and anisotropy in Rayleigh-Taylor turbulence" by Dongxiao Zhao, Riccardo Betti, and Hussein Aluie

## A. *Efficiency of the fluxes*

We have observed (figures 7-8 in the main text) that baropycnal work $\langle \Lambda_\ell \rangle$ dominates at the largest scales. It acts as a conduit for mean injection from potential energy by transferring energy from the largest scales to smaller scales in the inertial range where deformation work $\Pi$ takes over and dominates the cascade process.

Since this work is the first to investigate $\Lambda_\ell$ as a function of scale $\ell$, a basic question that arises is whether its decay at small $\ell$ is due to a decay in its magnitude or due to a mis-alignment of $\boldsymbol{\nabla}\overline{P}_\ell$ and $\overline{\tau}_\ell(\rho, \mathbf{u})$. We shall answer the question in this subsection. We first reiterate the flux expressions in equation (3.5) in the main text for convenience:

$$\Pi = -\bar{\rho}\partial_j \widetilde{u}_i \widetilde{\tau}(u_i, u_j) = -\bar{\rho}\widetilde{S}_{ij}\widetilde{\tau}(u_i, u_j)$$
$$\Lambda = \frac{1}{\bar{\rho}}\partial_i \overline{P}\overline{\tau}(\rho, u_i)$$

where $\widetilde{S}_{ij} = 1/2(\partial_i \widetilde{u}_j + \partial_j \widetilde{u}_i)$ is the Favre filtered velocity strain tensor. Following (Liao & Ouellette (2014); Fang & Ouellette (2016); Ballouz & Ouellette (2018)), we define the cascade efficiency $\Gamma_\Lambda$ and $\Gamma_\Pi$ to be

$$\begin{aligned} \Gamma_\Lambda &= \frac{\partial_i \bar{P}\ \overline{\tau}(\rho, u_i)}{(\partial_j \bar{P}\partial_j \bar{P})^{1/2}(\overline{\tau}(\rho, u_k)\overline{\tau}(\rho, u_k))^{1/2}} \\ \Gamma_\Pi &= -\frac{\widetilde{S}_{ij}\ \widetilde{\tau}(u_i, u_j)}{(\widetilde{S}_{kl}\widetilde{S}_{kl})^{1/2}(\widetilde{\tau}(u_m, u_n)\widetilde{\tau}(u_m, u_n))^{1/2}} \end{aligned} \tag{S-1}$$

which resembles the cosine of the angle between two vectors. These definitions in equation (S-1) follow that in Ballouz & Ouellette (2018) who studied the cascade efficiency in constant-density turbulence. By the Cauchy-Schwartz inequality, $-1 \leqslant \Gamma_\Lambda, \Gamma_\Pi \leqslant 1$.

Similarly, the magnitudes of these two fluxes, denoted by $M_\Lambda$ and $M_\Pi$, are defined by the denominator in the flux efficiency equation (S-1):

$$\begin{aligned} M_\Lambda &= (\partial_j \bar{P}\partial_j \bar{P})^{1/2}(\overline{\tau}(\rho, u_k)\overline{\tau}(\rho, u_k))^{1/2} \\ M_\Pi &= (\widetilde{S}_{kl}\widetilde{S}_{kl})^{1/2}(\widetilde{\tau}(u_m, u_n)\widetilde{\tau}(u_m, u_n))^{1/2} \end{aligned} \tag{S-2}$$

and can be regarded as the product of tensor magnitudes. The actual $\Pi$ and $\Lambda$ terms are proportional to the product of efficiency and magnitude

$$\Lambda \propto \Gamma_\Lambda \cdot M_\Lambda, \qquad \Pi \propto \Gamma_\Pi \cdot M_\Pi$$

with a proportionality factor involving density.

The cascade efficiency and magnitude of $\Lambda$ in 2D and 3D are shown in figure S1. Magnitude $M_\Lambda$ in both 2D and 3D decreases at smaller scales as appears in figures 1(b) and 1(d). In fact, figure S2(b) shows that $M_\Lambda$ seems to scale $\sim k^{-2/3}$. This decay can be understood from basic scaling estimates for the magnitude of $\Lambda = \frac{1}{\bar{\rho}}\nabla\overline{P}_\ell\overline{\tau}_\ell(\rho, \mathbf{u})$, following (Eyink (2007-2008, 2005); Aluie (2011)). We first observe that in our flows, both 2D and 3D, the pressure field is mostly smooth as evidenced by the scaling of its filtering spectrum in figure S2(a), decaying at least as fast† as $k^{-3}$, where $k$ is filtering wavenumber (inverse of scale). Therefore, the pressure gradient is dominated by the

† As Sadek & Aluie (2018) elaborate, the filtering spectrum for a field with actual scaling that is steeper than $k^{-3}$ will appear as $k^{-3}$ when using 1st-order filtering kernels such as a Gaussian.

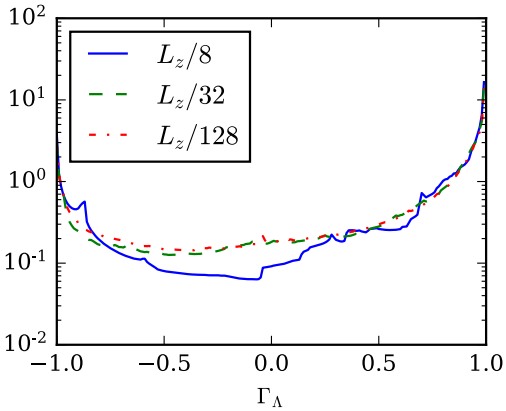


(a) PDF of $\Gamma_\Lambda$ in 2D-RT. Mean efficiency equals 0.50, 0.48, 0.44 for $\ell = L_z/8$, $L_z/32$, $L_z/128$, respectively.

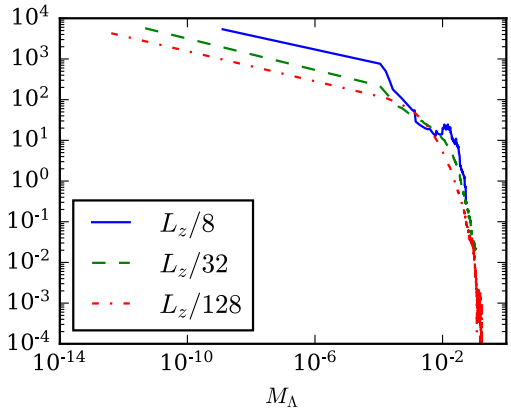


(b) PDF of $M_\Lambda$ in 2D-RT. Mean magnitude equals 7.8E-3, 3.7E-3, 1.68E-3 for $\ell = L_z/8$, $L_z/32$, $L_z/128$, respectively.

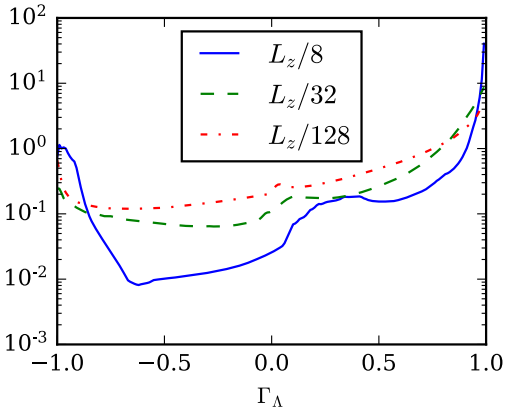


(c) PDF of $\Gamma_\Lambda$ in 3D-RT. Mean efficiency equals 0.71, 0.70, 0.54 for $\ell = L_z/8$, $L_z/32$, $L_z/128$, respectively.

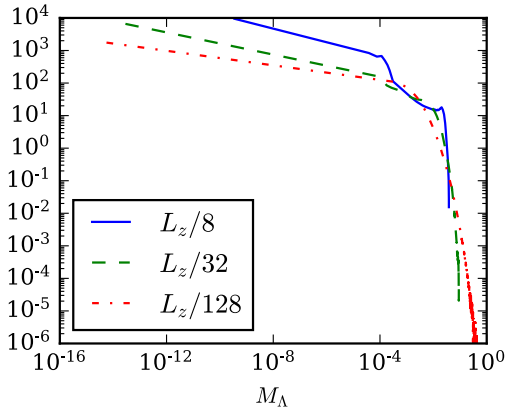


(d) PDF of $M_\Lambda$ in 3D-RT. Mean magnitude equals 6.1E-3, 3.0E-3, 1.2E-3 for $\ell = L_z/8$, $L_z/32$, $L_z/128$, respectively.

FIGURE S1. PDFs of the efficiency and magnitude of $\Lambda$ at different scales from the 2D4096 and 3D1024 data at time $\widehat{t} = 4$. The PDFs of efficiency are on a linear-log plot, while the PDFs of magnitude are on a log-log plot for clarity.

largest scale $L$,

$$\nabla \overline{P}_\ell \sim \frac{\delta P(L)}{L},$$

and is (to leading order) independent of $\ell$, where an increment is defined as usual, $\delta f(r) \equiv f(x+r) - f(x)$. Here, $L$ is a characteristic large scale of RT, comparable to the domain size. On the other hand, subscale mass flux scales as (Aluie (2011)):

$$\overline{\tau}_\ell(\rho, \mathbf{u}) \sim \delta\rho(\ell)\delta\mathbf{u}(\ell) \sim \ell^{\sigma_\rho + \sigma_u} \sim k^{-2/3}$$

where $\delta\rho(\ell) \sim \ell^{\sigma_\rho}$, $\delta\mathbf{u}(\ell) \sim \ell^{\sigma_u}$, and from figure 5, the two scaling exponents $\sigma_\rho \lessapprox 1/3, \sigma_u \gtrapprox 1/3$, yielding $\sigma_\rho + \sigma_u \approx 2/3$. This explains decay of $M_\Lambda$ as a function of filtering wavenumber $k_\ell = L_z/\ell$ in both 2D and 3D-RT. The decay is faster in the dissipation range since fluctuations giving rise to $\overline{\tau}_\ell(\rho, \mathbf{u})$ decay faster at those scales.

An important conclusion from the scaling of the pressure spectrum in figure S2(a) is

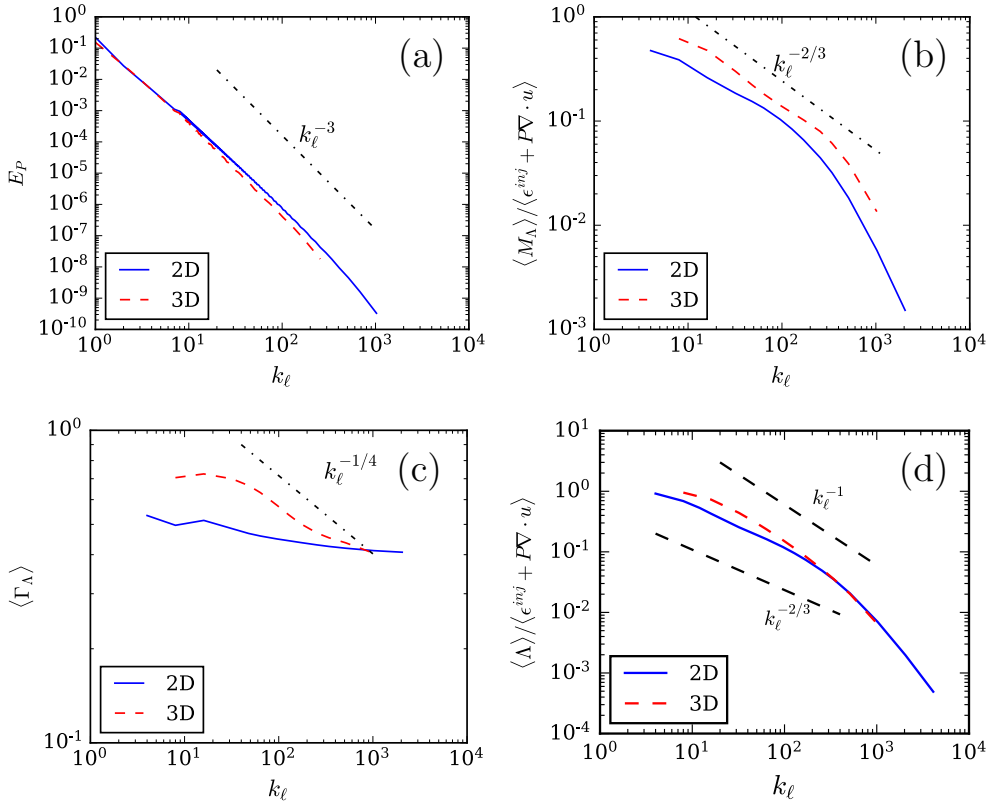


FIGURE S2. Explaining the decay of $\Lambda$ at small scales. (a) Filtering spectrum, $E_P$, of pressure using the 2D4096 and 3D1024 data at $\widehat{t}=4$. $E_P \equiv \frac{d}{dk}\langle|\overline{P}_\ell|^2\rangle$, where the $k_\ell$-derivative is in the filtering wavenumber $k_\ell = L_z/\ell$ following equation (2.13) in the main text. (b) Scaling of $M_\Lambda$ in 2D and 3D. The normalization, $\langle\epsilon^{\rm inj}+P\nabla\cdot\mathbf{u}\rangle$, is calculated from the corresponding 2D and 3D data. (c) Mean efficiency of $\Lambda$ as functions of scale in 2D & 3D, both of which show a weak dependence on $k_\ell$. (d) Decay of $\langle\Lambda\rangle$ in 2D & 3D as functions of scale.

that energy transfer by $\Lambda$ is (infrared) non-local in scale due to dominance of the largest scale $L$ in the pressure gradient (Eyink (2005); Eyink & Aluie (2009); Aluie (2011)). This is similar to energy transfer in the Batchelor range of magnetohydrodynamic turbulence at high magnetic Prandtl numbers (Batchelor (1959); Aluie & Eyink (2010)), where energy is transferred nonlocally from the flow at viscous scales $\ell_\nu$ to the magnetic field at much smaller scales due to smoothness of the velocity at those small viscous scales. We note, however, that such non-local transfer by $\Lambda$ is mostly likely a hallmark of RT turbulence, where $\boldsymbol{\nabla}P$ is dominated by the largest scales in the system, and may not hold in general variable density turbulence in which the pressure field is not smooth (Aluie (2011)).

While the magnitude $M_\Lambda$ decays at smaller scales both in 2D-RT and 3D-RT, efficiency $\Gamma_\Lambda$ seems to have a much weaker decay at small scales. Figure S1(a) shows that $\Gamma_\Lambda$ in 2D-RT is almost independent of scale, which is reinforced by scaling plots in figure S2(c). In 3D-RT, figure S2(c) shows a very shallow scaling, with $\langle\Gamma_\Lambda\rangle \sim k_\ell^{-1/4}$.

To explain the decay of $\langle\Lambda\rangle$ at small scales we observed in 2D-RT (figure 7 in the main text) and in 3D-RT (figure 8 in the main text), we assume that the efficiency and magnitude of $\Lambda$ are statistically independent, $\langle\Lambda\rangle \sim \langle\Gamma_\Lambda\rangle\langle M_\Lambda\rangle$ (within the factor $\frac{1}{\bar{\rho}}$).

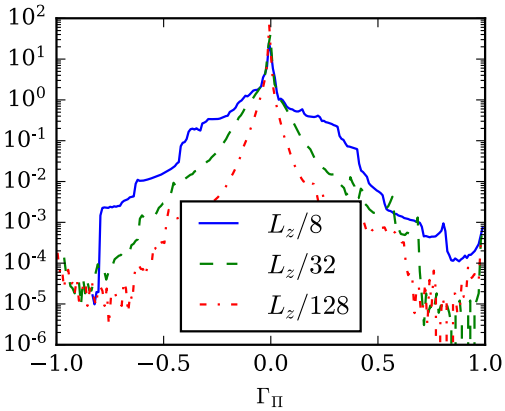


(a) PDF of $\Gamma_\Pi$ in 2D-RT. Mean efficiency equals -0.018, -0.012, -0.0092 for $\ell = L_z/8$, $L_z/32$, $L_z/128$, respectively.

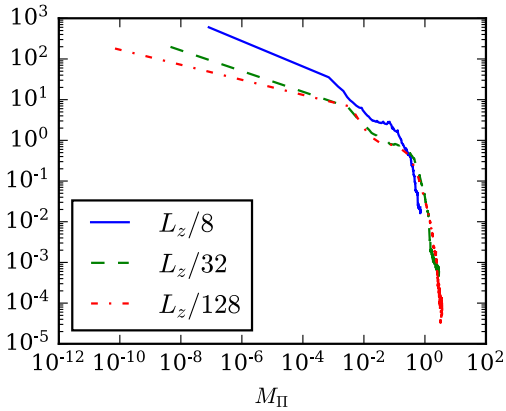


(b) PDF of $M_\Pi$ in 2D-RT. Mean magnitude equals 0.064, 0.11, 0.093 for $\ell = L_z/8$, $L_z/32$, $L_z/128$, respectively.

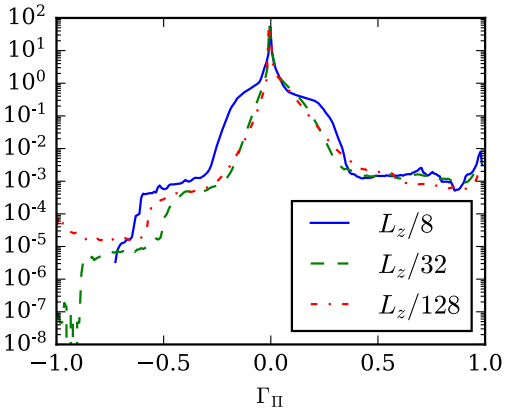


(c) PDF of $\Gamma_\Pi$ in 3D-RT. Mean efficiency equals 2E-3, 5E-3, 2.2E-3 for $\ell = L_z/8$, $L_z/32$, $L_z/128$, respectively.

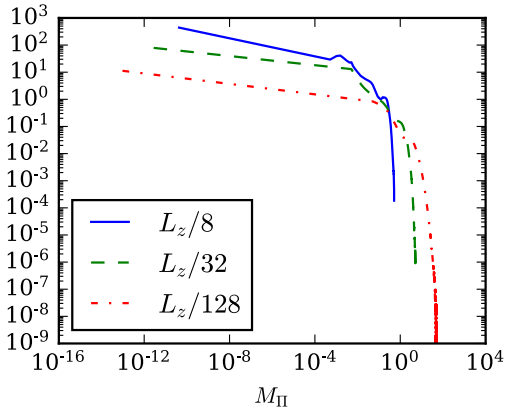


(d) PDF of $M_\Pi$ in 3D-RT. Mean magnitude equals 5.5E-2, 0.26, 0.75 for $\ell = L_z/8$, $L_z/32$, $L_z/128$, respectively.

FIGURE S3. PDFs of the efficiency and magnitude of $\Pi$ at different scales from the 2D4096 and 3D1024 data at time $\widehat{t} = 4$. The PDFs of efficiency are on a linear-log plot, while the PDFs of magnitude are on a log-log plot for clarity.

When this is combined the above observations on the scaling of each of $M_\Lambda$ and $\Gamma_\Lambda$, we are able to explain the decay of $\langle \Lambda \rangle$, which figure S2(d) shows to be $\sim k_\ell^{-2/3}$ in 2D and $\sim k_\ell^{-1}$ in 3D. Therefore, we can conclude from the foregoing discussion that the decay in $\langle \Lambda_\ell \rangle$ at smaller $\ell$ is primarily due to a decay in its magnitude rather than due to a mis-alignment of $\boldsymbol{\nabla}\overline{P}_\ell$ and $\overline{\tau}_\ell(\rho, \mathbf{u})$.

Unlike $\Lambda$, which decays monotonically in the inertial range, deformation work $\Pi$ peaks in the inertial range as it takes over the energy transfer process. PDFs of the efficiency of $\Pi$ (figures S3(a),(c)) indicate a profound difference from $\Lambda$. Whereas the PDFs of $\Gamma_\Lambda$ in figures S2(a) and (c) peak around the maximum possible values, -1 and 1, $\Gamma_\Pi$ has a highest probability around zero. This is consistent with the investigation by Ballouz & Ouellette (2018), who concluded that $\Pi$ is inefficient at transferring energy in constant-density homogeneous turbulence (see also Fang & Ouellette (2016)). Thus, the $\Pi$ flux, which transfers energy due to subscale stress acting against a larger-scale strain, is less

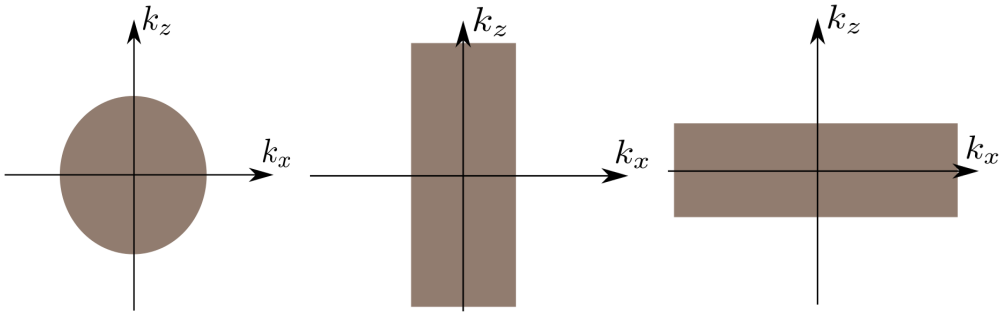


(a) Isotropic filtering (b) Anisotropic filtering with $G_\ell^x$ (c) Anisotropic filtering with $G_\ell^z$

FIGURE S4. Schematics of isotropic and anisotropic filtering, associated with scale $\ell$. Filtering is performed in physical space to disentangle scales, without resorting to Fourier transforms. Filtering wavenumbers $\mathbf{k} = (k_x, k_z) = (L/\ell_x, L/\ell_z)$ are only a proxy for length-scales, but may be thought of as Fourier wavenumbers conceptually. (a) Isotropic (low-pass) filtering with kernel $G_\ell$ retains scales within the shaded sphere in (scale) k-space, satisfying $|\mathbf{k}| \leqslant L/\ell$. (b) Anisotropic filtering with kernel $G_\ell^x$ retains scales within the shaded slab in (scale) k-space, satisfying $|k_x| \leqslant L/\ell$ without decomposing scales in the z-direction. (c) Anisotropic filtering with kernel $G_\ell^z$ retains scales within the shaded slab in (scale) k-space, satisfying $|k_z| \leqslant L/\ell$ without decomposing scales in the x-direction.

efficient than $\Lambda$, which operates by the barotropic and baroclinic generation of vorticity and strain (Lees & Aluie (2019); Zhao *et al.* (in preparation)).

## B. $\Pi$ *and* $\Lambda$ *with anisotropic filters*

In section 4 of the main text, we analyzed how the fluxes can lead to anisotropic motion in different directions by directional splitting of the kinetic energy budget, which we coarse-grained with isotropic kernels. In this section, we shall quantify the *anisotropy of length-scales* energized by $\Pi$ and $\Lambda$, through coarse-graining with anisotropic kernels. We use the following 'horizontal kernel' and 'vertical kernel':

$$G_\ell^x(\mathbf{x}) = \left(\frac{6}{\pi\ell^2}\right)^{1/2} e^{-\frac{6}{\ell^2}x^2}, \quad G_\ell^z(\mathbf{x}) = \left(\frac{6}{\pi\ell^2}\right)^{1/2} e^{-\frac{6}{\ell^2}z^2}$$

which perform the filtering operation in only one direction. These filters only capture the spectral information in the corresponding direction and ignore variations in the other directions. We denote the fluxes calculated by these anisotropic kernels using notation such as $\Pi_{G_x}$ or $\Lambda_{G_z}$. Note that unlike the 'directionally split' analysis presented earlier, here the sum of anisotropically filtered fluxes does not equal the full flux, i.e., $\Lambda_{G_x} + \Lambda_{G_y} + \Lambda_{G_z} \neq \Lambda$.

The essence of isotropic and anisotropic filtering is illustrated in figure S4 in $k$-space, where filtering wavenumbers $\mathbf{k} = (k_x, k_z) = (L/\ell_x, L/\ell_z)$ are only a proxy for length-scales, but can be conceptually associated with Fourier wavenumbers commonly used in the community. Here, $L$ is any characteristic large-scale to be used only as a *common* reference in all directions to define filtering wavenumbers. Figure S4 depicts a two-dimensional wavenumber space, with horizontal and vertical filtering wavenumbers corresponding to scales in the x-direction and z-direction, respectively. Isotropic filtering with kernel $G_\ell$ retains scales within the shaded sphere in $k$-space (figure 4(a)), satisfying $|\mathbf{k}| \leqslant L/\ell$. On the other hand, anisotropic filtering with kernel $G_\ell^x$, for example, retains scales within the shaded slab in $k$-space (figure 4(b)), satisfying $|k_x| \leqslant L/\ell$ but does not

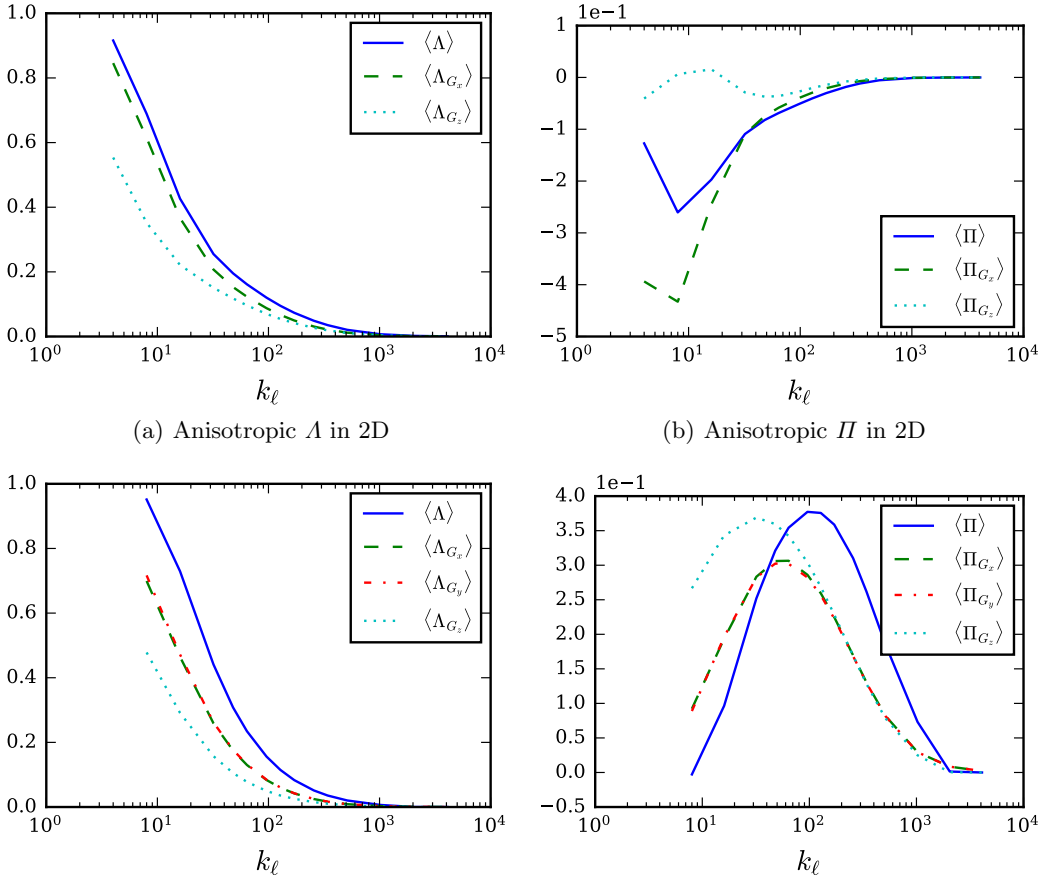


(a) Anisotropic $\Lambda$ in 2D (b) Anisotropic $\Pi$ in 2D

(c) Anisotropic $\Lambda$ in 3D (d) Anisotropic $\Pi$ in 3D

FIGURE S5. Probing scale anisotropy of fluxes $\Lambda_G$ and $\Pi_G$ using the 2D4096 and 3D1024 data at $\widehat{t} = 4.0$. Filtering wavenumber is $k_\ell = L_z/\ell$. Plots are normalized by $\langle \epsilon^{\text{inj}} + P\nabla\cdot\mathbf{u}\rangle$ at the corresponding time. Energy transfer across horizontal and vertical scales are shown alongside energy transferred isotropically in scale space.

allow us to probe scales in the z-direction since it does not partition those scales. The analysis generalizes to 3D in a straightforward way.

Mean anisotropic fluxes of the 2D4096 and 3D1024 data, at time $\widehat{t} = 4.0$, are shown in figure S5. For baropycnal work $\Lambda$, both the 2D and 3D results shown in figures 5(a) and 5(c) indicate that $\langle\Lambda_{G_x}\rangle$ is larger than $\langle\Lambda_{G_z}\rangle$. This implies that most of the potential energy is being transferred to horizontal scales, although nonzero transfer is also creating flow variation in the vertical direction. The tendency of baropycnal transfer in energizing small-scales along the x-direction is consistent with our understanding of RT instability during the linear stage when potential energy feeds perturbations that vary in the horizontal direction. Figures 5(a),5(c) indicate that baropycnal transfer from potential energy at later times, when the flow becomes nonlinear, also participates in the creation of vertical scales. This is consistent with the association of baropycnal work with vorticity and strain creation (Lees & Aluie (2019)), which necessarily involve small-scales in the vertical direction. Nevertheless, horizontal scale creation still dominates at late times, with $\langle\Lambda_{G_x}\rangle > \langle\Lambda_{G_z}\rangle$ at all scales. Note that in 3D, we have $\langle\Lambda_{G_x}\rangle \approx \langle\Lambda_{G_y}\rangle$

in figure 5(c), indicating that horizontal scales are being energized isotropically by $\Lambda$, as expected.

Probing anisotropy of deformation work $\Pi$, we can observe significant differences between the 2D case, shown in figure 5(b), and the 3D case, shown in figure 5(d). In 2D, the mean value of $\Pi$ calculated from isotropic kernel is negative, and so is the anisotropic $\Pi_{G_x}$. On the other hand, mean $\Pi_{G_z}$ attains positive values over a certain range of scales. Since $\Pi = -\overline{\rho}\partial_j\widetilde{u}_i\widetilde{\tau}(u_i, u_j)$ is primarily determined by the velocity fields, we shall focus on the characteristics of velocity fields in RT evolution. The positive $\langle\Pi_{G_z}\rangle$ measures energy transfer across vertical scales, which goes into sustaining the 'mixing fronts,' which are the two envelopes enclosing the mixing layer in RT turbulence. We verified this from visualizations of $\Pi_{G_z}$ (not shown here). This is similar to the downscale energy transfer that forms and sustains the shock front in a 1D Burgers flow. In our RT flow, the velocity profile along the z-axis comprises of a vertical flow inside the mixing layer pushing against a more quiescent fluid outside. Such fronts necessarily involve small vertical scales that need to be constantly replenished by $\Pi$, otherwise the front would broaden. We find that inside the mixing layer (not shown), away from the fronts, $\Pi_{G_z} < 0$, transferring net energy upscale as in a homogeneous 2D flow. However, the contribution from the front regions is stronger such that overall $\langle\Pi_{G_z}\rangle > 0$. Despite being positive, $\langle\Pi_{G_z}\rangle$ is much smaller than the net upscale transfer in the horizontal direction measured by $\langle\Pi_{G_x}\rangle$ in figure 5(b), which dominates the cross-scale transfer when we treat all directions equally by using isotropic kernels to measure $\langle\Pi\rangle$ in figure 5(b). In the 3D-RT flow, we see in figure 5(d) that $\Pi_{G_x}$, $\Pi_{G_y}$, and $\Pi_{G_z}$ are all positive, transferring energy downscale. We find that $\Pi_{G_z}$ peaks at slightly larger scales and again plays a role in the formation of the mixing fronts as in 2D, while $\langle\Pi_{G_x}\rangle \approx \langle\Pi_{G_y}\rangle \geqslant 0$, indicating isotropic downscale transfer in the horizontal scales.

We also note that $\langle\Pi_{G_z}\rangle > \langle\Pi_{G_x}\rangle$ at all scales, indicating that the 'mixing front' propagation plays an important role in the downscale kinetic energy transfer. This aspect of energy transfer was missing in previous studies relying on FFTs in the horizontal while neglecting vertical scales.

## C. *Filtering Spectra of Kinetic Energy*

Here, we compare the 'filtering' spectra using three different scale-decompositions to define kinetic energy, following Zhao & Aluie (2018). In variable density flows, scale decomposition is not as straightforward as in constant density flows. One possible decomposition is to define large-scale kinetic energy as $\overline{\rho}_\ell|\overline{\mathbf{u}}_\ell|^2/2$, which has been used in many studies (e.g. Chassaing (1985); Bodony & Lele (2005); Burton (2011); Karimi & Girimaji (2017)). Another possibility is to define large-scale kinetic energy as $|\overline{(\sqrt{\rho}\mathbf{u})}_\ell|^2/2$, which has also been used extensively in compressible turbulence studies (e.g. Kida & Orszag (1990); Cook & Zhou (2002); Wang *et al.* (2013); Grete *et al.* (2017)). A third is based on the Favre decomposition (Hesselberg (1926); Favre (1958)), which we adopt in this work, and uses $\overline{\rho}_\ell|\widetilde{\mathbf{u}}_\ell|^2/2$ as the definition for large-scale kinetic energy, where $\widetilde{\mathbf{u}}_\ell(\mathbf{x}) = \overline{\rho\mathbf{u}}_\ell/\overline{\rho}_\ell$.

Zhao & Aluie (2018) demonstrated numerically that these three different quantities, all of which have units of energy, are governed by different dynamics. Specifically, it was shown that for large $\ell$, viscous dissipation is negligible for the Favre decomposition but significant for the other two in a variety of flows; normal 1D shock, 2D-RT and 3D-RT, subject to a dynamic viscosity that is either constant or temperature-dependent.

Following Sadek & Aluie (2018), the filtering spectra for the three definitions are:

$$E_F(k_\ell) \equiv \frac{d}{dk_\ell}\langle \overline{\rho}_\ell |\widetilde{\mathbf{u}}_\ell(\mathbf{x})|^2\rangle/2 \tag{S-3}$$

$$E_C(k_\ell) \equiv \frac{d}{dk_\ell}\langle \overline{\rho}_\ell |\overline{\mathbf{u}}_\ell(\mathbf{x})|^2\rangle/2 \tag{S-4}$$

$$E_K(k_\ell) \equiv \frac{d}{dk_\ell}\langle |\overline{(\sqrt{\rho}\mathbf{u})}_\ell(\mathbf{x})|^2\rangle/2 \tag{S-5}$$

where $k_\ell = L/\ell$, $L$ is the domain size of interest, $\ell$ is the scale we are probing, and $\langle\cdot\rangle$ stands for spatial averaging. Subscript 'F' stands for Favre, while 'C' and 'K' denote the lead authors of papers in which those definitions, to our best knowledge, first appeared (Chassaing (1985); Kida & Orszag (1990)).

Figure S6 compares these three spectra using the high Atwood RT simulations in 2D and 3D. We find discernible differences from the 2D2048high simulation but not from the 3D512high data. We suspect the lack of differences from the 3D512high data may be due to an enhanced microscopic mixing between the heavy and light fluids at late times. We observe (not shown) that differences among the definitions using the 3D512high data were relatively larger at earlier times, albeit still small in absolute terms, especially when compared to those from the 2D2048high data. Microscopic mixing in 2D-RT is much smaller than in 3D-RT as observed in previous studies (e.g. Cabot 2006), due to weaker small inertial scales as we discussed in the main text above.

With $\mathcal{A} = 0.8$, our flows have an initial density ratio of $\rho_h/\rho_l = 9$. Achieving higher ratios in a well-resolved turbulence simulation is computationally challenging, especially in 3D (e.g. Livescu & Ristorcelli (2008)). Yet, many flows of interest have much larger density ratios, reaching of up to 600 laboratory flow experiments (Read (1984); Dimonte & Schneider (2000)), typically exceeding $10^4 - 10^5$ in laboratory fusion plasmas (e.g. Craxton *et al.* (2015); Yan *et al.* (2016); Zhang *et al.* (2020)), and ranging from $10^6$ to $10^{20}$ in molecular clouds in the interstellar medium (e.g. Kritsuk *et al.* (2007); Federrath *et al.* (2010); Pan *et al.* (2016)). The most ubiquitous terrestrial two-fluid mixing is between air and water which have a density ratio of 1000.

Since we are testing possible differences among the definitions, which can be applied to any density and velocity fields regardless of their dynamical origin, we synthetically increase the density contrast Zhao & Aluie (2018) in the flows we are analyzing by taking powers of the density, $A\,\rho^8(\mathbf{x})$, as a post-processing step, then normalizing the resultant field such that the total mass in the domain is the same as in the original flow, $\langle\rho\rangle = A\,\langle\rho^8\rangle$. Note that this is not based on physical grounds, but serves to highlight differences among the three decompositions under higher density contrasts.

Figure S6 (right column) compares these three spectra using $A\,\rho^8(\mathbf{x})$ as a density field and original velocity from the high Atwood RT simulations in 2D and 3D. We now find more pronounced differences among the three decompositions, especially from the 2D2048high data; $E_C(k_\ell)$ from equation (S-4) decays rapidly at high $k_\ell$, while $E_K(k_\ell)$ from equation (S-5) becomes shallower than the Favre-based spectrum $E_F(k_\ell)$ (equation (S-3)), scaling similar to $k^{-5/3}$ even in 2D.

The purpose of Figure S6 is to demonstrate that filtering spectra based on different kinetic energy decompositions can differ. It is not our intention here to argue which is more physical, which was the subject of previous studies (Zhao & Aluie (2018); Aluie (2013)).

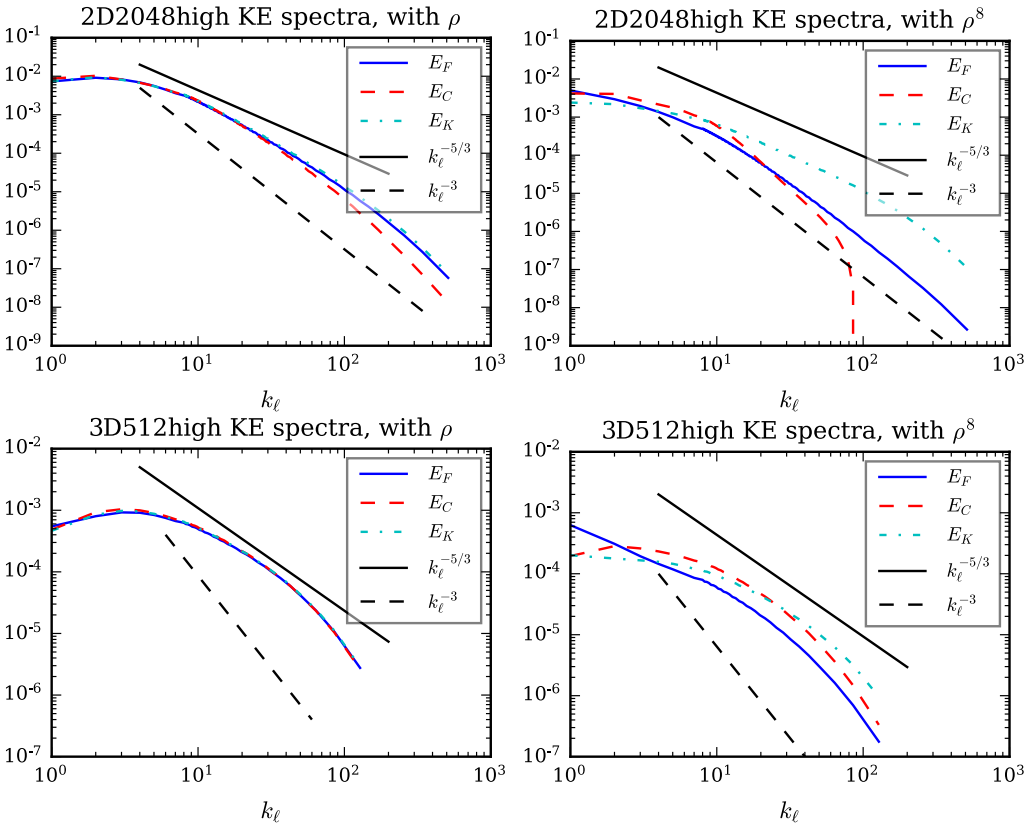


FIGURE S6. Filtering spectra of kinetic energy using three different scale-decompositions (eqs. (S-3)-(S-5)). Top and bottom rows use 2D-RT and 3D-RT data, respectively. Left column uses the raw density field, $\rho$. Right column usesq $\rho^8$ (normalized to conserve mass) to highlight differences among the definitions under an increased density contrast. Data from 2D2048high was at $\hat{t} = 4.4$. Data from 3D512high was at $\hat{t} = 4.0$.

### D. *2D-RT simulation with same initial condition as in 3D1024*

For verification purpose, we performed two additional 2D turbulent RT simulations (see Table 1); run 2D1024 of grid size $1024 \times 2048$ and run 2D2048 on a $2048 \times 4096$ grid. Both have the same initial perturbations as in 3D1024. Specifically, the vertical velocity field is perturbed at the interface in wavenumber space within the wavenumber annulus $k \in [32, 128]$, with amplitude proportional to $e^{-\frac{1}{c}|k_x^2 - 80^2|}$, where $c \approx 22.63$ is a normalization constant to further limit the range of effectively perturbed wavenumber. We shall see that the analysis performed on these results are consistent with those obtained from run 2D4096 in the main text.

Figure S7 shows the mixing width $h(t)$ versus time, with $\alpha = 0.034$ for 2D1024, and $\alpha = 0.037$ for 2D2048, which are similar to 2D4096 in figure 3 with $\alpha = 0.036$. Figure S8 shows the corresponding instantaneous and overall kinetic energy budgets, which is similar to the 2D4096 case shown in figure 4(a) and 4(b). The KE budget as a function of scale is shown in figure S9, which resembles the 2D4096 result in figure 7 of the main text. The temporal self-similarity of the new 2D1024 and 2D2048 RT fluxes also holds, and is shown in figure S10, similar to those in the 2D4096 case in figure 11 of the main text. All the analysis presented here is consistent with the results from run 2D4096 in

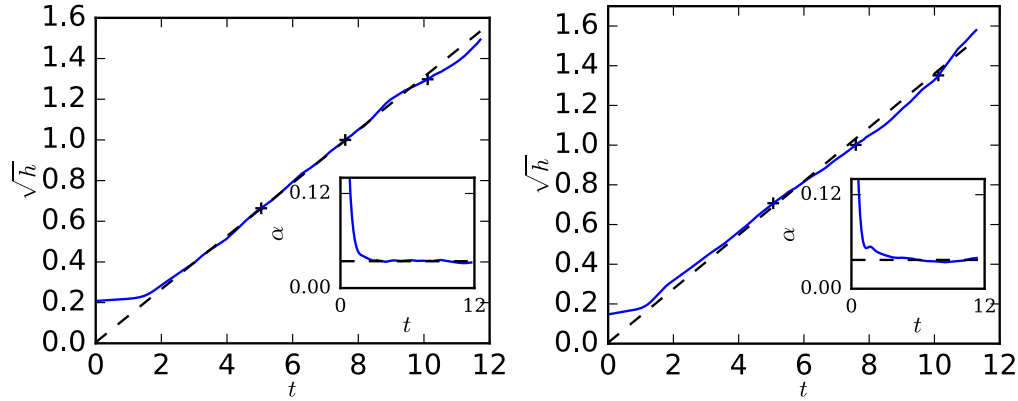


FIGURE S7. Similar to figure 3 of the main text, the square root of mixing width $\sqrt{h(t)}$ versus time for the new 2D-RT simulations. Left figure is for 2D1024, with $\alpha = 0.034$, and right figure is for 2D2048, with $\alpha = 0.037$. The '+' markers correspond to dimensionless time $\widehat{t} = t/\sqrt{\frac{L_x}{\mathcal{A}g}} = 2, 3, 4$. Inset: the compensated plot $\alpha = \frac{h(t)}{\mathcal{A}gt^2}$ versus time, in which the horizontal lines correspond to the $\alpha$ value obtained by linear fit.

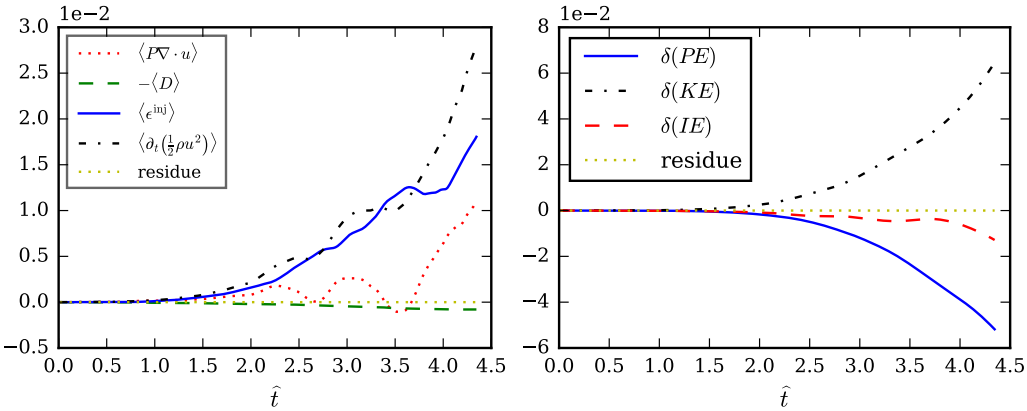


(a) 2D1024 instantaneous budget




(b) 2D1024 overall budget

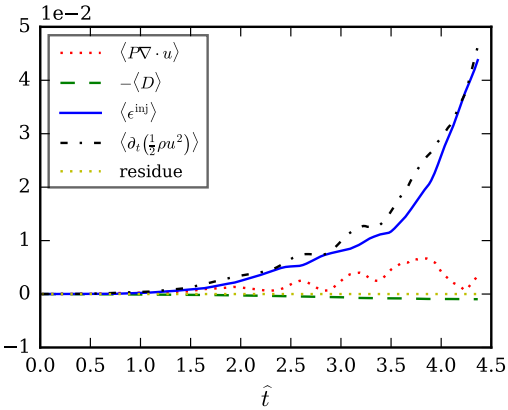


(c) 2D2048 instantaneous budget

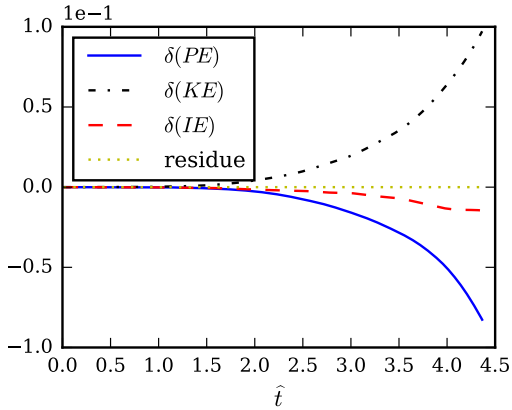


(d) 2D2048 overall budget

FIGURE S8. Temporal evolution of kinetic energy budget, and overall energy balance for 2D1024 in (a)-(b), and 2D2048 in (c)-(d), similar to figure 4(a) and 4(b) of the main text.

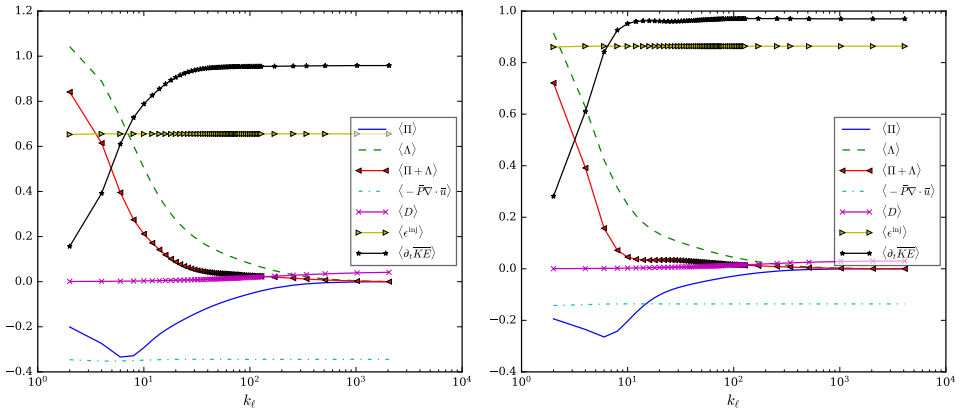


FIGURE S9. Similar to figure 7 of the main text, mean kinetic energy budget as a function of scale in 2D at dimensionless time $\widehat{t} = 4.0$. Left figure is for 2D1024 and right figure for 2D2048. The plots are normalized by $\langle \epsilon^{\rm inj} + P\nabla\cdot\mathbf{u}\rangle$, the available mean source of kinetic energy.

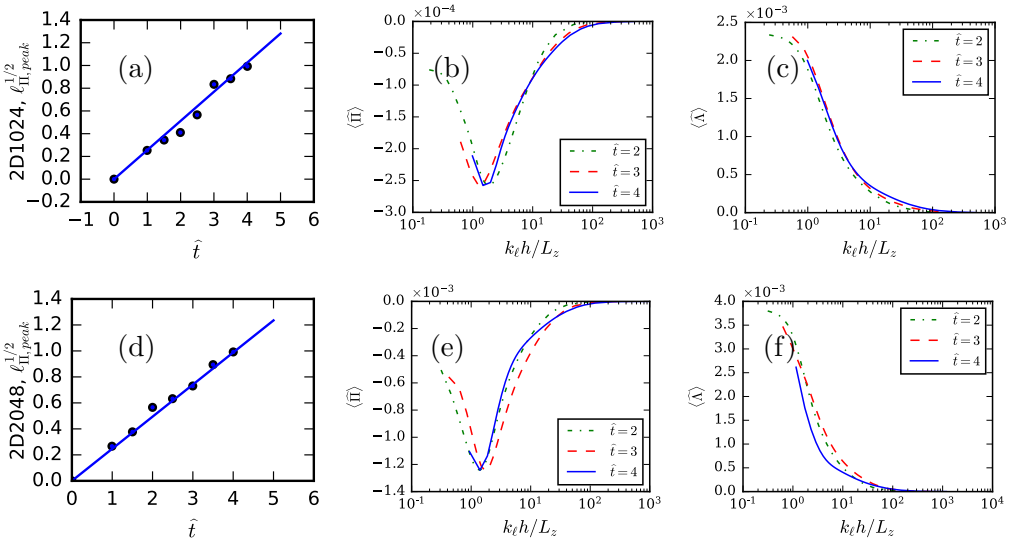


FIGURE S10. Similar to figure 11 of the main text, the temporal self-similarity of turbulent RT fluxes for the new 2D-RT simulations. Panels (a)-(c) are 2D1024 results, and panels (d)-(f) are 2D2048 results. Panels (a), (d) plot length scale $\ell_{\Pi,\rm peak}$ associated with the peak of $\Pi$ versus dimensionless time $\widehat{t}$. Panels (b), (e) show rescaled $\langle\widehat{\Pi}\rangle$ in equation (3.7). Panels (c), (f) show rescaled $\langle\widehat{\Lambda}\rangle$.

the main text, implying that the slight difference in initial conditions between 2D4096 and 3D1024 does not affect our conclusions.

## E. *Another form of kinetic energy budget*

In the compressible turbulence LES modeling literature, another formulation of the Favre filtered large scale kinetic energy budget, similar to equation (3.1) of the main text, is often used. In this formulation, pressure dilatation is lumped with the $\Lambda$ term by the relation:

$$-\Lambda_\ell + \overline{P}_\ell \nabla\cdot\overline{\mathbf{u}}_\ell = \overline{P}\nabla\cdot\widetilde{\mathbf{u}}_\ell + \nabla\cdot\left[\overline{P}(\overline{\mathbf{u}}_\ell - \widetilde{\mathbf{u}}_\ell)\right] \tag{S-6}$$

using the identity (Aluie (2011))

$$\widetilde{\mathbf{u}}_\ell = \overline{\mathbf{u}} + \frac{\overline{\tau}(\rho, \mathbf{u})}{\overline{\rho}}$$

Thus, the filtered large and small scale kinetic energy equations, and the filtered internal energy equation are:

$$\begin{aligned}
&\partial_t \bar{\rho}_\ell \frac{|\widetilde{\boldsymbol{u}}_\ell|^2}{2} + \nabla\cdot[\cdots] = \bar{P}_\ell \nabla\cdot\widetilde{\boldsymbol{u}}_\ell + \cdots \\
&\partial_t \frac{\bar{\rho}_\ell \widetilde{\tau}_\ell(u_i, u_i)}{2} + \nabla\cdot[\cdots] = (\overline{P\nabla\cdot\mathbf{u}} - \bar{P}\nabla\cdot\widetilde{\mathbf{u}}) + \cdots \\
&\partial_t \overline{\rho e}_\ell + \nabla\cdot[\cdots] = -\bar{P}_\ell \nabla\cdot\widetilde{\mathbf{u}}_\ell - (\overline{P\nabla\cdot\mathbf{u}}_\ell - \bar{P}_\ell\nabla\cdot\widetilde{\mathbf{u}}_\ell) + \cdots
\end{aligned} \tag{S-7}$$

the omitted terms are similar to those in our formulation of the coarse-grained budgets in equation (3.1) of the main text. Many previous works on compressible turbulence adopt the framework of equation (S-7), see Lele (1994) and the references therein. There are a few exceptions, such as in Huang *et al.* (1995), in which they preferred to have a separate $\Lambda$ based on modelling considerations that density weighted decomposition should only be applied to the convective terms, and also in (Aluie (2011, 2013); Wang *et al.* (2013); Eyink & Drivas (2018)) where it was argued that $\Lambda$ and $\bar{P}\nabla\cdot\bar{\mathbf{u}}$ are fundamentally different from a physics standpoint since the former has contributions from scales both larger and smaller than $\ell$ and represents the interaction between different scales, while the latter only involves large scale quantities.

We remark that these two formulations, equation (3.1) of the main text and equation (S-7), are mathematically equivalent but represents different interpretations of the scale processes, which is illustrated schematically in figure S11 (in which potential energy and dissipation have been omitted for clarity). In figure S11, there are three channels for energy transfer: i) between internal energy (IE) and large scale kinetic energy (KE), ii) between IE and small scale KE, and iii) between large and small scale KE. For each channel, the energy transfer is different between the two interpretations, but the total energy transferred between IE and KE (when summing both large scales and small scales) is the same and equals to $\overline{P\nabla\cdot\mathbf{u}}$, as can be readily checked from the sum of the values associated with the arrows in both figures. However, an important distinction is that in the second formulation in figure 11(b), mean pressure dilatation acts over a much wider range of scales, preventing a simple understanding of the flow in terms of inertial range dynamics. This is illustrated with solid arrows in coupling internal energy to KE at scales both large and small, which can hinder the unraveling of inertial range dynamics. We thus advocate for using our formulation in equation (3.1) of the main text.

## References

Aluie, H. 2011 Compressible Turbulence: The Cascade and its Locality. *Phys. Rev. Lett.* **106** (17), 174502.

Aluie, Hussein 2013 Scale decomposition in compressible turbulence. *Physica D: Nonlinear Phenomena* **247** (1), 54–65.

Aluie, H. & Eyink, G. 2010 Scale Locality of Magnetohydrodynamic Turbulence. *Phys. Rev. Lett.* **104** (8), 081101.

Ballouz, Joseph G & Ouellette, Nicholas T 2018 Tensor geometry in the turbulent cascade. *Journal of Fluid Mechanics* **835**, 1048–1064.

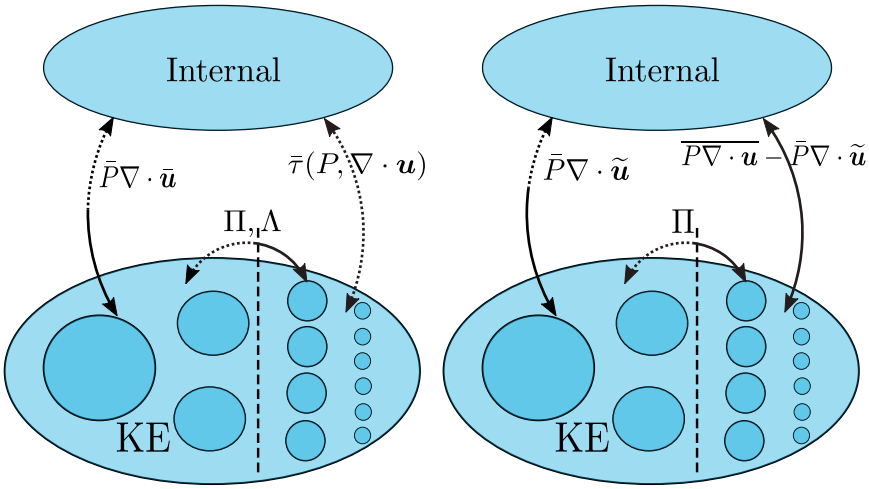


(a) Energy pathways by equation (3.1) (b) Energy pathways by equation (S-7)

FIGURE S11. Two formulations of energy pathways according to equation (3.1) of the main text and equation (S-7). *Kinematically possible* pathways are depicted with dashed arrows, while those that are *dynamically manifested* are depicted with solid arrows. (a) Internal energy (IE) is coupled to large scale KE via $\bar{P}\nabla\cdot\bar{\mathbf{u}}$, and large scale KE transfers to small scale KE via both $\Pi$ and $\Lambda$. At small scales, IE is channeled to KE at the rate $\bar{\tau}(P,\nabla\cdot\mathbf{u})$, but this pathway is found to be dynamically inactive (see figures 7,8 and discussion in sections 3.2.3-3.2.4 of the main text). (b) According to the formulation common in LES, IE is coupled to large scale KE via $\bar{P}\nabla\cdot\widetilde{\mathbf{u}}$, and large scale KE transfers to small scale KE only via $\Pi$ ($\Lambda$ is absent). At small scales, IE is channeled to KE at the rate $\overline{P\nabla\cdot\mathbf{u}}-\bar{P}\nabla\cdot\widetilde{\mathbf{u}}$, which unlike our formulation, is a dynamically significant pathway since its mean equals $\langle\Lambda\rangle+\langle\bar{\tau}(P,\nabla\cdot\mathbf{u})\rangle$ (see equation (S-6)), incorrectly suggesting that pressure dilatation is important at small scales in RT flows. Other terms such as dissipation and injection are not shown here for clarity. The main difference between the two formulations is that IE is coupled to KE at both large and small scales in (b), which can hinder the unraveling of inertial range dynamics.

BATCHELOR, GEORGE K 1959 Small-scale variation of convected quantities like temperature in turbulent fluid part 1. general discussion and the case of small conductivity. *Journal of Fluid Mechanics* **5** (1), 113–133.

BODONY, DANIEL J & LELE, SANJIVA K 2005 On using large-eddy simulation for the prediction of noise from cold and heated turbulent jets. *Physics of Fluids* **17** (8), 085103.

BURTON, GREGORY C 2011 Study of ultrahigh Atwood-number Rayleigh–Taylor mixing dynamics using the nonlinear large-eddy simulation method. *Physics of Fluids* **23** (4), 045106.

CABOT, W 2006 Comparison of two-and three-dimensional simulations of miscible rayleigh-taylor instability. *Physics of Fluids* **18** (4), 045101.

CHASSAING, P 1985 An alternative formulation of the equations of turbulent motion for a fluid of variable density. *Journal de Mecanique Theorique et Appliquee* **4**, 375–389.

COOK, ANDREW W & ZHOU, YE 2002 Energy transfer in Rayleigh-Taylor instability. *Physical Review E* **66** (2), 192.

CRAXTON, R S, ANDERSON, K S, BOEHLY, T R, GONCHAROV, V N, HARDING, D R, KNAUER, J P, MCCRORY, R L, MCKENTY, P W, MEYERHOFER, D D, MYATT, J F, SCHMITT, A J, SETHIAN, J D, SHORT, R W, SKUPSKY, S, THEOBALD, W, KRUER, W L, TANAKA, K, BETTI, R, COLLINS, T J B, DELETTREZ, J A, HU, S X, MAROZAS, J A, MAXIMOV, A V, MICHEL, D T, RADHA, P B, REGAN,

S P, Sangster, T C, Seka, W, Solodov, A A, Soures, J M, Stoeckl, C & Zuegel, J D 2015 Direct-drive inertial confinement fusion: A review. *Physics of Plasmas* **22** (11), 110501.

Dimonte, G & Schneider, M 2000 Density ratio dependence of Rayleigh-Taylor mixing for sustained and impulsive acceleration histories. *Physics of Fluids* **12** (2), 304–321.

Eyink, Gregory L 2005 Locality of turbulent cascades. *Physica D: Nonlinear Phenomena* **207** (1), 91–116.

Eyink, Gregory L 2007-2008 Turbulence theory course notes. `http://www.ams.jhu.edu/~eyink/Turbulence/`.

Eyink, Gregory L & Aluie, Hussein 2009 Localness of energy cascade in hydrodynamic turbulence. i. smooth coarse graining. *Physics of Fluids* **21** (11), 115107.

Eyink, Gregory L & Drivas, Theodore D 2018 Cascades and dissipative anomalies in compressible fluid turbulence. *Physical Review X* **8** (1), 011022.

Fang, Lei & Ouellette, Nicholas T 2016 Advection and the Efficiency of Spectral Energy Transfer in Two-Dimensional Turbulence. *Physical Review Letters* **117** (10), 104501.

Favre, A. 1958 Équations statistiques des gaz turbulents: Masse, quantité de mouvement. *C. R. Acad. Sci. Paris* **246**, 2576–2579.

Federrath, C, Roman-Duval, J, Klessen, R S, Schmidt, W & Mac Low, M M 2010 Comparing the statistics of interstellar turbulence in simulations and observations. *Astronomy & Astrophysics* **512**, A81.

Grete, Philipp, O'Shea, Brian W, Beckwith, Kris, Schmidt, Wolfram & Christlieb, Andrew 2017 Energy transfer in compressible magnetohydrodynamic turbulence. *Physics of Plasmas* **24** (9), 092311.

Hesselberg, T. 1926 Die Gesetze der ausgeglichenen atmosphärischen Bewegungen. *Beiträge zur Physik der freien Atmosphäre* **12**, 141–160.

Huang, PG, Coleman, GN & Bradshaw, P 1995 Compressible turbulent channel flows: Dns results and modelling. *Journal of Fluid Mechanics* **305**, 185–218.

Karimi, Mona & Girimaji, Sharath S 2017 Influence of orientation on the evolution of small perturbations in compressible shear layers with inflection points. *Physical Review E* **95** (3).

Kida, Shigeo & Orszag, Steven A 1990 Energy and spectral dynamics in forced compressible turbulence. *Journal of Scientific Computing* **5** (2), 85–125.

Kritsuk, Alexei G, Norman, Michael L, Padoan, Paolo & Wagner, Rick 2007 The statistics of supersonic isothermal turbulence. *Astrophysical Journal* **665** (1), 416–431.

Lees, Aarne & Aluie, Hussein 2019 Baropycnal work: A mechanism for energy transfer across scales. *Fluids* **4** (2), 92.

Lele, Sanjiva K 1994 Compressibility effects on turbulence. *Annual review of fluid mechanics* **26** (1), 211–254.

Liao, Yang & Ouellette, Nicholas T 2014 Geometry of scale-to-scale energy and enstrophy transport in two-dimensional flow. *Physics of Fluids* **26** (4), 045103.

Livescu, Daniel & Ristorcelli, JR 2008 Variable-density mixing in buoyancy-driven turbulence. *Journal of Fluid Mechanics* **605**, 145–180.

Pan, Liubin, Padoan, Paolo, Haugbølle, Troels & Nordlund, Åke 2016 Supernova Driving. II. Compressive Ratio In Molecular-Cloud Turbulence. *The Astrophysical Journal Letters* **825** (1), 30.

Read, KI 1984 Experimental investigation of turbulent mixing by rayleigh-taylor instability. *Physica D: Nonlinear Phenomena* **12** (1-3), 45–58.

Sadek, Mahmoud & Aluie, Hussein 2018 Extracting the spectrum of a flow by spatial

filtering. *Physical Review Fluids* **3** (12), 124610.

Wang, Jianchun, Yang, Yantao, Shi, Yipeng, Xiao, Zuoli, He, XT & Chen, Shiyi 2013 Cascade of kinetic energy in three-dimensional compressible turbulence. *Physical review letters* **110** (21), 214505.

Yan, R, Betti, R, Sanz, J, Aluie, H, Liu, B & Frank, A 2016 Three-dimensional single-mode nonlinear ablative rayleigh-taylor instability. *Physics of Plasmas* **23** (2), 022701.

Zhang, Huasen, Betti, R, Yan, Rui & Aluie, H 2020 Nonlinear bubble competition of the multimode ablative Rayleigh–Taylor instability and applications to inertial confinement fusion. *Physics of Plasmas* **27** (12), 122701.

Zhao, Dongxiao & Aluie, Hussein 2018 Inviscid criterion for decomposing scales. *Physical Review Fluids* **3** (5), 054603.

Zhao, Dongxiao, Betti, Riccardo & Aluie, Hussein in preparation Energy pathways in single-mode rayleigh-taylor flows .